

# [2,2']Paracyclophane-Based $\pi$ -Conjugated Molecular Wires Reveal Molecular-Junction Behavior

Agustín Molina-Ontoria,<sup>†</sup> Mateusz Wielopolski,<sup>‡</sup> Julian Gebhardt,<sup>‡</sup> Andreas Gouloumis,<sup>†</sup> Timothy Clark,<sup>§</sup> Dirk M. Guldi,<sup>\*,†</sup> and Nazario Martín<sup>\*,†,||</sup>

<sup>†</sup>Departamento de Química Orgánica, Facultad de Química, Universidad Complutense, E-28040 Madrid, Spain

<sup>‡</sup>Department of Chemistry and Pharmacy and Interdisciplinary Center for Molecular Materials (ICMM), Friedrich-Alexander-Universität Erlangen-Nürnberg, Egerlandstrasse 3, 91058 Erlangen, Germany

<sup>§</sup>Computer-Chemie-Centrum, Cluster of Excellence Engineering of Advanced Materials, University of Erlangen, Nögelsbachstrasse 25, 91052 Erlangen, Germany

<sup>||</sup>Facultad de Ciencias, IMDEA-Nanociencia, Campus Cantoblanco, E-28049 Madrid, Spain

**S** Supporting Information

**ABSTRACT:** The electronic coupling as well as the attenuation factor ( $\beta$ ), which depends primarily on the nature of the molecular bridge and is used as a benchmark to test the molecular wire behavior, have been determined in a systematic study carried out on a series of ZnP/C<sub>60</sub> conjugates connected through a [2,2']paracyclophane-oligophenylenevinylene (pCp-oPPV). The convergent synthesis involves a series of Horner–Emmons olefination reactions or double palladium-catalyzed Heck-type reactions. ZnP–pCp–C<sub>60</sub> conjugates were finally obtained by the 1,3-dipolar cycloaddition reaction of the in situ-generated azomethyne ylide containing the ZnP–pCp moiety to the [60]fullerene using Prato conditions. Experimental (UV–vis, fluorescence, transient absorption spectroscopy, and solution electrochemistry) and theoretical studies revealed that the pCps act as molecular junctions. If hole transfer is assumed to be the dominant charge transfer (CT) mechanism, CT is facilitated in one direction (from C<sub>60</sub> to ZnP via pCp) but disfavored in the other direction (from ZnP to C<sub>60</sub> via pCp).

$\pi$ -Conjugated organic molecules have been widely used for studying charge-transport processes in solution and/or the solid state.<sup>1</sup> In this context, electronic coupling/communication with a length dependence that is directly related to the electronic properties of the individual constituents (electron donor, bridge, and electron acceptor) is decisive.<sup>1</sup> Efficient charge transport is in fact realized only when the synergy between different parts leads to “molecular wire” behavior, which describes  $\pi$ -conjugated molecules capable of transporting charges efficiently over length scales far beyond those of chemical bonds.<sup>2</sup>

For short molecular bridges, resonant-tunneling electron transfer leads to an exponential dependence on the length<sup>3</sup> described by  $k = k_0 e^{-\beta R}$ , where  $R$  is the distance between the electroactive constituents and  $\beta$  is the attenuation factor, which depends primarily on the nature of the molecular bridge. For long molecular bridges, the relationship between the length and

the rate constant becomes linear because the weaker length dependence associated with the hopping regime facilitates the transport of charges over sizable distances.  $\beta$  quantifies the charge transfer (CT) capability of the bridge and in turn is a bridge-specific parameter. As such, it depends both on the magnitude of the electronic coupling between the electron donor and electron acceptor and on the energy of the localized CT states (i.e., electron or hole).

Recent work on  $\pi$ -conjugated electron donor–acceptor conjugates has provided a wealth of information.<sup>4</sup> However, relatively little is known about the physicochemical features of  $\pi$  systems that contain subunits with strong through-space interactions, such as [2,2']paracyclophane (pCp). In pCp, the close proximity of the arene moieties results in strong electronic and structural interactions between the two rings. As a consequence, styryl[2,2']paracyclophane derivatives exhibit highly conductive behavior due to efficient through-space  $\pi$ – $\pi$  coupling.<sup>5</sup>

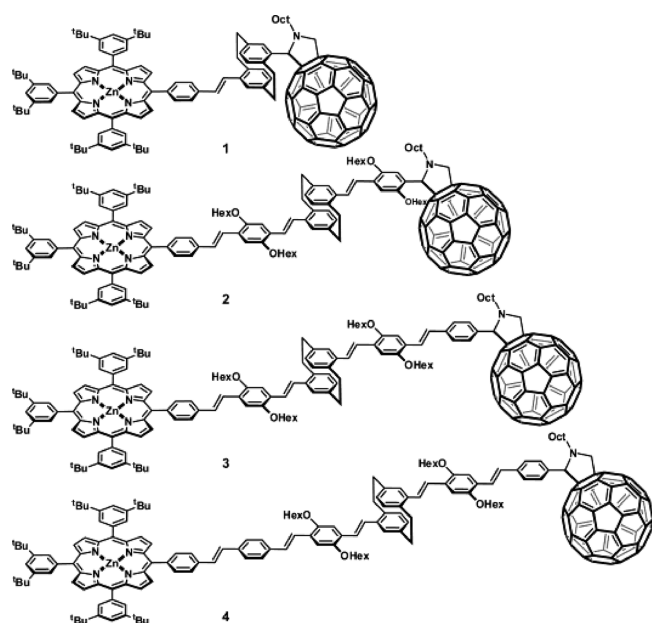
In the current investigation, on the basis of our previous work on charge transport, that is, charge separation and charge recombination through molecular wires,<sup>6</sup> we have bridged a series of ZnP–C<sub>60</sub> conjugates by [2,2']paracyclophane–oligophenylenevinylene (pCp-oPPV)  $\pi$  systems having different lengths. Neither the magnitude of electronic coupling nor the attenuation factor between electron donors and electron acceptors linked by pCps has previously been determined.

Compounds 1–4 (Chart 1; for details, see the Supporting Information) were prepared using 4,12-diformylparacyclophane<sup>7</sup> (5) in the case of 1 or pCps bearing substituted bis-benzaldehydes (10) for 2–4. In the first step, these were coupled to a zinc porphyrin (ZnP) using a procedure similar to that previously reported for related endohedral fullerenes.<sup>8</sup> In the second step, the correspondingly formed monoaldehydes were attached to C<sub>60</sub> via a 1,3-dipolar cycloaddition reaction.<sup>9</sup> The synthesis of precursor monoaldehyde 14 for the preparation of 3 was carried out by consecutive Wittig and Heck reactions (see the Supporting Information).

**Received:** November 12, 2010

**Published:** February 7, 2011

Chart 1. Different ZnP–pCp–C<sub>60</sub> Triads (1–4) Prepared in This Work



The solution electrochemistry of **1–4** was studied using cyclic voltammetry at room temperature and compared with that of ZnP and C<sub>60</sub>–pCp, as shown in Figure S1 and Tables S1 and S2 in the Supporting Information. They are all electrochemically active in both the anodic and cathodic scan directions. In the cathodic scans, **1–4** exhibit four reductions at  $-0.84$ ,  $-1.42$ ,  $-1.79$ , and  $-2.04$  V. The first, second, and fourth reversible one-electron reductions agree reasonably well with the C<sub>60</sub> reduction in C<sub>60</sub>–pCp. The third quasi-reversible one-electron reduction, on the other hand, corresponds to the ZnP reduction and is in excellent agreement with that seen for ZnP itself. In the anodic scan, only the quasi-reversible one-electron oxidation of ZnP emerges at  $0.53$  V. In short, the redox features of **1–4** are simply the superimposition of those seen for the references. This leads us to conclude that no significant electronic interactions between the different redox- and photoactive constituents exist in the ground state.

The UV–vis absorption spectra of **1–4** are dominated by the Soret and Q bands of ZnP at  $430$  and  $550/604$  nm, respectively (Figure S2). Characteristic absorptions of C<sub>60</sub> and pCp–oPPV are found in the UV region and show a significant overlap. In particular, C<sub>60</sub> absorbs between  $250$  and  $320$  nm, whereas the broad pCp–oPPV absorption maximum in THF gradually shifts from  $304$  to  $329$  nm. In comparison with the absorption of pristine oPPVs of equal length, the absorption maxima of pCp–oPPV are blue-shifted by  $\sim 20$  nm. This suggests weaker  $\pi$  conjugation across the pCp core. All three component moieties (ZnP, pCp–oPPV, and C<sub>60</sub>) emit singlet excited state energy in different regions of the solar spectrum. While the fluorescence of ZnP is typically observed in the region between  $600$  and  $700$  nm, pCp–oPPVs emit between  $430$  and  $550$  nm. The C<sub>60</sub> emission with its maximum at  $715$  nm is, however, masked by the stronger ZnP emission; quantum yields for these processes are  $6.0 \times 10^{-4}$  and  $4.0 \times 10^{-2}$ , respectively. Interestingly, in THF, the ZnP-centered fluorescence is appreciably quenched (Figure S3) in all of the ZnP–pCp–oPPV–C<sub>60</sub> conjugates, regardless of the system being excited into the Soret- or Q-band region; the

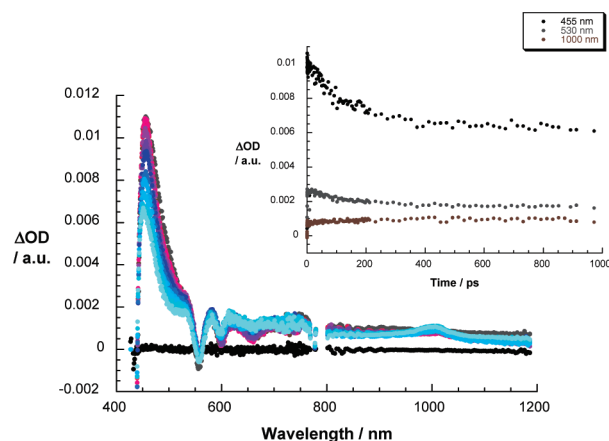
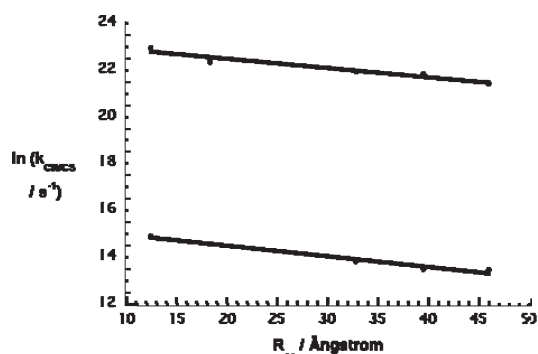


Figure 1. Differential absorption spectra (visible and near-IR) obtained upon femtosecond flash photolysis ( $420$  nm,  $90$  nJ) of **3** in argon-saturated THF with several time delays between  $0$  and  $3000$  ps at room temperature. Inset: corresponding time profiles at  $455$ ,  $530$ , and  $1000$  nm that monitor the charge-separation dynamics.

quantum yields are  $4.0 \times 10^{-3}$  for **1**,  $1.6 \times 10^{-2}$  for **2**,  $1.9 \times 10^{-2}$  for **3**, and  $2.6 \times 10^{-2}$  for **4**. This suggests that there are sizable interactions between the strongly fluorescent ZnP and electron-accepting C<sub>60</sub> units in the excited state. Increasing the solvent polarity by using benzonitrile strengthens the fluorescence quenching. In contrast, increasing the donor–acceptor separation weakens it. In complementary time-resolved measurements, we determined ZnP fluorescence lifetimes of  $200$ ,  $930$ ,  $1270$ , and  $1700$  ps for **1**, **2**, **3**, and **4**, respectively. The latter are a quantitative match of the fluorescence quantum yields.

Complementary transient absorption measurements were used to investigate the nature of the deactivation processes evolving from photoexcitation. The characteristic features due to singlet excited states of the references **11** and **19** (see the Supporting Information) are, for example, formed instantaneously. In the case of pCp–oPPV, singlet–singlet absorptions develop that include a transient bleach between  $430$  and  $500$  nm and a broad transient maximum at  $600$  nm (Figure S4). Characteristics of the ZnP singlet excited state are a bleach around  $560$  nm and transients at  $480$  nm and between  $580$  and  $750$  nm. Fast intersystem-crossing processes ( $10^{11}$  s<sup>−1</sup>) govern the fate of the singlet excited states in **11** and **19** and lead to the triplet manifolds. The singlet excited state lifetimes of **11** and **19** were determined to  $21$  and  $56$  ps, respectively. The corresponding triplet–triplet absorptions were found as broad transients between  $500$  and  $900$  nm (Figure S4).

Moving on to the donor–acceptor systems **1–4**, we focused on the generation of the singlet excited states of ZnP. In accordance with previous publications, however, we may safely assume that starting with the C<sub>60</sub> singlet excited state would lead to similar reaction patterns.<sup>10</sup> At the very beginning of the experiments, the transient absorption spectra of **1–4** were those found for the instantaneous formation of the ZnP singlet excited state. However, instead of the fast intersystem crossing dynamics and growth of the triplet, we saw that the singlet–singlet absorption decayed quickly in the presence of C<sub>60</sub> (Figure 1). The singlet excited state lifetimes ranged from  $200$  ps for **1** to  $830$  ps for **2**,  $1430$  ps for **3**, and  $1890$  ps for **4**, resembling the corresponding fluorescence lifetimes. At the end of the singlet decay, new transient features emerged with maxima in the



**Figure 2.** Dependence of the charge-separation ( $k_{\text{CS}}$ ) and charge-recombination ( $k_{\text{CR}}$ ) rate constants on the center-to-center separation ( $R_{\text{CC}}$ ) in nitrogen-saturated THF at room temperature for the directly connected 1–4. The slopes represent the  $\beta$  values.

visible (580–710 nm) and near-IR (800–1200 nm) regions. The visible maxima at 480, 580, and 620 nm correspond to the one-electron-oxidized  $\pi$ -radical cation of ZnP ( $\text{ZnP}^{\bullet+}$ ), while the near-IR maximum at 1000 nm resembles the signature of the one-electron-reduced form of  $\text{C}_{60}$  ( $\text{C}_{60}^{\bullet-}$ ). In other words, the fast deactivation of the ZnP singlet excited state is linked to the formation of the  $\text{ZnP}^{\bullet+}$ –pCp–oPPV– $\text{C}_{60}^{\bullet-}$  radical ion pair state. Although we cannot rule out the presence of the triplet markers for  $\text{C}_{60}$  at 700 nm (see Figure S5) and ZnP at 840 nm (see Figure S4), their formation is unlikely to occur because of their high energies of  $\sim 1.5$  eV. In other words, the radical ion pair states, with energies of 1.35 eV for 1, 1.40 eV for 2, 1.40 eV for 3, and 1.42 eV for 4, are sufficiently below the two triplets.<sup>11</sup>

The  $\text{ZnP}^{\bullet+}$ –pCp–oPPV– $\text{C}_{60}^{\bullet-}$  radical ion pair state lifetimes exceeded the time scale of our femtosecond experiments (3 ns) and were determined in nanosecond experiments. The spectral fingerprints of the  $\text{ZnP}^{\bullet+}$ –pCp–oPPV– $\text{C}_{60}^{\bullet-}$  radical ion pair state, as seen immediately after the nanosecond laser pulse, were useful probes in this context (Figure S6). The kinetics of the  $\text{ZnP}^{\bullet+}$ –pCp–oPPV– $\text{C}_{60}^{\bullet-}$  radical ion pair state decays obeyed clean unimolecular rate laws. In strictly oxygen-free THF, the lifetimes are 466 ns for 1, 974 ns for 2, 1373 ns for 3, and 1422 ns for 4.

The contrast between the fast charge-separation processes [i.e.,  $5.2 \times 10^9 \text{ s}^{-1}$  (1),  $3.4 \times 10^9 \text{ s}^{-1}$  (2),  $3.1 \times 10^9 \text{ s}^{-1}$  (3), and  $2.1 \times 10^9 \text{ s}^{-1}$  (4)] and the slow charge-recombination processes [i.e.,  $2.2 \times 10^6 \text{ s}^{-1}$  (1),  $1.0 \times 10^6 \text{ s}^{-1}$  (2),  $7.3 \times 10^5 \text{ s}^{-1}$  (3), and  $7.0 \times 10^5 \text{ s}^{-1}$  (4)] leads us to conclude that the two processes are located in the normal and inverted regions of the Marcus parabola, respectively. In this context, the small reorganization energy of  $\text{C}_{60}$  in electron-transfer reactions is certainly decisive. However, the facts that pCps interrupt the homogeneous through-bond  $\pi$  conjugation in oPPVs on the one hand and institute strong through-space  $\pi$ – $\pi$  coupling interactions on the other hand are equally important.

Thus, we postulate that low-lying, through-space delocalized states facilitate CT in one direction (i.e., charge separation) but retard it in the opposite one (i.e., charge recombination). Consequently, we analyzed the dependence of the CT rate constants on the donor–acceptor separation. Figure 2 shows the resulting plots. Their slopes give  $\beta$  values of  $0.039 \pm 0.001 \text{ \AA}^{-1}$  for charge separation and  $0.045 \pm 0.001 \text{ \AA}^{-1}$  for charge recombination.



**Figure 3.** Visualization of the electrostatic potentials of the BS states of 2, 3, and 4.

Further insight into the electronic conduction across the pCp linkage was provided by molecular orbital (MO) calculations. Figure S7 shows that the HOMO and LUMO are localized on ZnP and  $\text{C}_{60}$ , respectively. Increased localization of the electron density on the pCp–oPPV bridge is found for the lower-energy orbitals (HOMO-1 to HOMO-3). In 1, the space between the donor and acceptor is fully conjugated because of the short donor–acceptor distance, as indicated by the orbital coefficients. The HOMO-2 orbital extends over the bridge. Increasing the pCp–oPPV length in 2–4 changes the situation. While the HOMO/HOMO-1 and LUMO remain localized on ZnP and  $\text{C}_{60}$ , respectively, the HOMO-2 and HOMO-3 are localized exclusively on the pCp–oPPVs. Importantly, no electron density can be found across the pCps, demonstrating the interruption of through-bond  $\pi$ -conjugation.

Configuration interaction (CI) calculations in a simulated solvent environment (diethyl ether) indicated that the presence of pCps leads to localized bridge CT states (BS states), which are stabilized within the  $\pi$ -electron framework of the oPPVs and are nearly degenerate (i.e., within  $\sim 2 \text{ kcal mol}^{-1}$ ) with the CT states (Table S3). In these bridge states, the positive charge actually resides on the pCps, and the stabilization within the  $\text{ZnP}$ –pCp–oPPV– $\text{C}_{60}$  systems is apparently stronger on  $\text{C}_{60}$ , as shown in Figure 3.

As Table S3 shows, these states contribute to the overall CT mechanisms because of their relatively low energies. Further, we note that in our CI calculations, excitations from the HOMO-2 and HOMO-3 orbitals made the greatest contributions to the CT states (see Table S4). Together with the fact that these orbitals lie within 0.1 eV of each other, we may confirm that the through-space conjugation in the pCps is sufficient to guarantee efficient coupling between the two sides of the pCp cores (Table S4).

In view of the fact that hole transport dominates the charge transport in  $\pi$ -conjugated molecular wires,<sup>12</sup> these states may act as intermediate steps in the CT process since they are stabilized by smaller changes of the dipole moment. On the basis of these results, we postulate that the pCps act as molecular junctions: CT in one direction (from  $\text{C}_{60}$  via pCp to ZnP) is facilitated, whereas it is disfavored in the opposite direction (from ZnP via pCp to  $\text{C}_{60}$ ).

Moreover, the local ionization potentials of 2–4 (Figure S8) show low values (green) around the bonds of the bridge, whereas high values (orange) are centered on the phenyl rings of the bridge. This suggests that hole transfer is favored along a homogeneous pathway of easily oxidizable sites.

Finally, a comparison of the CT behavior of the pCp–oPPV linkers to fully conjugated oPPV systems<sup>6</sup> clearly visualizes



the effects of the pCp units. The 20 nm blue shift of the pCp-oPPV absorption maxima relative to the oPPV absorptions (discussed above; see Figure S2) hints at weaker  $\pi$ -conjugation of the pCp-oPPVs due to through-space interactions across pCp. Similarly, visualization the HOMO-2 and HOMO-3 (Figure S7) confirm the fact that at larger bridge lengths, the pCps break the through-bond conjugation. In the end, these effects are reflected in a  $\beta$  value that is  $\sim 4$  times greater than that for fully conjugated oPPV bridges (i.e., 0.04 in pCp-oPPV vs 0.01 in oPPV). Additionally, the inhomogeneous coupling due to the pCp units leads to different  $\beta$  values for charge separation and charge recombination. In the oPPVs, on the other hand, the extremely homogeneous distribution of  $\pi$  electrons along the bridge results in equal transport properties for both directions (i.e., charge separation and charge recombination).

## ■ ASSOCIATED CONTENT

**S Supporting Information.** Experimental procedures and complete spectroscopic and structural analysis, including Figures S1–S8. This material is available free of charge via the Internet at <http://pubs.acs.org>.

## ■ AUTHOR INFORMATION

### Corresponding Author

[dirk.guldi@chemie.uni-erlangen.de](mailto:dirk.guldi@chemie.uni-erlangen.de); [nazmar@quim.ucm.es](mailto:nazmar@quim.ucm.es)

## ■ ACKNOWLEDGMENT

Financial support by the MEC of Spain (Projects CTQ2008-0795/BQU and Consolider-Ingenio 2010C-07-25200), the CAM (MADRISOLAR-2 Project S2009/PPQ-1533), the EU (FUNMOL FP7-212942-1), and the Deutsche Forschungsgemeinschaft (SFB 583 and Clusters of Excellence Engineering of Advanced Materials) is acknowledged. A.M.-O. and A.G., thank the CAM for a research grant and the MEC of Spain for a Ramón y Cajal Contract, respectively.

## ■ REFERENCES

- (1) (a) Nitzan, A.; Ratner, M. A. *Science* **2003**, *300*, 1384. (b) Davis, W. B.; Svec, W. A.; Ratner, M. A.; Wasielewski, M. R. *Nature* **1998**, *396*, 60. (c) Choi, S. H.; Kim, B.-S.; Frisbie, D. C. *Science* **2008**, *320*, 1482.
- (2) (a) Roberston, N.; McCowan, C. A. *Chem. Soc. Rev.* **2003**, *32*, 96. (b) Sikes, H. D.; Smalley, J. F.; Dudek, S. P.; Cook, A. R.; Newton, M. D.; Chidsey, C. E. D.; Feldberg, S. W. *Science* **2001**, *291*, 1519.
- (3) (a) Conwell, E. M. *Proc. Natl. Acad. Sci. U.S.A.* **2005**, *102*, 8795. (b) Giese, B. *Acc. Chem. Res.* **2000**, *33*, 631.
- (4) (a) James, D. K.; Tour, J. M. *Top. Curr. Chem.* **2005**, *257*, 33. (b) Weiss, E. A.; Wasielewski, M. R.; Ratner, M. A. *Top. Curr. Chem.* **2005**, *257*, 103. (c) Guldi, D. M.; Illescas, B. M.; Atienza, C. M.; Wielopolski, M.; Martín, N. *Chem. Soc. Rev.* **2009**, *38*, 1587.
- (5) (a) Seferos, D. S.; Trammell, S. A.; Bazan, G. C.; Kushmerick, J. G. *Proc. Natl. Acad. Sci. U.S.A.* **2005**, *102*, 8821. (b) Bartholomew, G. P.; Bazan, G. C. *Acc. Chem. Res.* **2001**, *34*, 30. (c) Kahnt, A.; Guldi, D. M.; de la Escosura, A.; Martínez-Díaz, M. V.; Torres, T. *J. Mater. Chem.* **2008**, *18*, 77.
- (6) (a) Giacalone, F.; Segura, J. L.; Martín, N.; Guldi, D. M. *J. Am. Chem. Soc.* **2004**, *126*, 5340. (b) de la Torre, G.; Giacalone, F.; Segura, J. L.; Martín, N.; Guldi, D. M. *Chem.—Eur. J.* **2005**, *11*, 1267. (c) Atienza, C.; Martín, N.; Wielopolski, M.; Haworth, N.; Clark, T.; Guldi, D. M. *Chem. Commun.* **2006**, 3202. (d) Atienza-Castellanos, C.; Wielopolski, M.; Guldi, D. M.; van der Pol, C.; Bryce, M. R.; Filippone, S.; Martín, N. *Chem. Commun.* **2007**, 5164. (e) Molina-Ontoria, A.; Fernández, G.; Wielopolski, M.; Atienza, C.; Sánchez, L.; Gouloumis, A.; Clark, T.; Martín, N.; Guldi, D. M. *J. Am. Chem. Soc.* **2009**, *131*, 12218.
- (7) Morisaki, Y.; Lin, L.; Chujo, Y. *Chem. Lett.* **2009**, *38*, 734.
- (8) Wolfrum, S.; Pinzón, J. R.; Molina-Ontoria, A.; Gouloumis, A.; Martín, N.; Echegoyen, L.; Guldi, D. M. *Chem. Commun.*, in press.
- (9) Prato, M.; Maggini, M. *Acc. Chem. Res.* **1998**, *31*, 519.
- (10) Giacalone, F.; Segura, J. L.; Martín, N.; Ramey, J.; Guldi, D. M. *Chem.—Eur. J.* **2005**, *11*, 4819.
- (11) Energies are based on the Born dielectric continuum model of the solvent as estimated using the expression by Weller (see: Weller, A. *Z. Phys. Chem. (Munich)* **1982**, *133*, 93).
- (12) (a) Xue, Y.; Datta, S.; Ratner, M. A. *J. Chem. Phys.* **2001**, *115*, 4292. (b) Derosa, P. A.; Seminario, J. M. *J. Phys. Chem. B* **2001**, *105*, 471. (c) Taylor, J.; Brandbyge, M.; Stokbro, K. *Phys. Rev. Lett.* **2002**, *89*, No. 138301.